Pergamon

Geochimica et Cosmochimica Acta, Vol. 65, No. 8, pp. 1219–1231, 2001

0016-7037/01 $20.00 + .00

PII S0016-7037(00)00564-0

An experimental study of enstatite dissolution rates as a function of pH, temperature, and aqueous Mg and Si concentration, and the mechanism of pyroxene/pyroxenoid dissolution

ERIC H. OELKERS* and JACQUES SCHOTT

Géochimie: Transferts et Mécanismes, CNRS/URM 5563—Université Paul Sabatier, 38 rue des Trente-six Ponts, 31400 Toulouse, France

(*Received December* 31, 1999; *accepted in revised form August* 16, 2000)

Abstract—Steady state enstatite dissolution rates, at far from equilibrium conditions, were measured as a function of aqueous magnesium and silica activity, pH from 1 to 11, and temperature from 28°C to 168°C. All rates were measured in mixed flow reactors and exhibited stoichiometric dissolution. Rates at pH = 2 are independent of aqueous silica activity, but decrease with increasing aqueous magnesium activity; constant temperature rates decrease continuously with increasing pH over the whole investigated pH range. All measured rates can be described within experimental uncertainty using

$$r = A_A \exp(-E_A/RT)(a^2_{H^+}/a_{Mg^{2+}})^{1/8}$$

where r signifies the enstatite steady state dissolution rate, A_A refers to a pre-exponential factor equal to 2.4×10^{-4} (mol of enstatite)/cm^2/s, E_A designates an activation energy equal to 48.5 kJ/mol, R represents the gas constant, and T denotes absolute temperature.

The variation of these rates with solution composition is interpreted to originate from the enstatite dissolution mechanism. The enstatite structure consists of silica tetrahedra chains that are branched together by magnesium octahedra. Mg–O bonds apparently break more rapidly than Si–O bonds in this structure. The breaking of Mg–O bonds, however, does not destroy the enstatite structure; it only partially liberates the silica tetrahedral chains by removing adjoining Mg atoms. Enstatite dissolution proceeds via (1) magnesium releasing exchange reactions between two aqueous H^+ and Mg in the enstatite structure, followed by (2) the relatively slow detachment of silica from partially liberated tetrahedral chains. The rate is proportional to the concentration of partially detached Si tetrahedra on the enstatite surface, which is linked through the law of mass action for the Mg/proton exchange reaction to aqueous magnesium activity and pH. Due to their similar structure and reaction rate dependencies on solution composition, it is postulated that the pyroxene/pyroxenoid minerals exhibit similar dissolution mechanisms to that proposed for enstatite. *Copyright © 2001 Elsevier Science Ltd*

1. INTRODUCTION

The motivation for this study is the improved understanding of the dissolution rates and mechanism of the pyroxene/pyroxenoid minerals. The weathering of the pyroxene/pyroxenoids are major contributors of Mg, Fe, and Ca to soils and surface waters (Drever, 1988; Drever and Clow, 1995). In soils, these metals are essential nutrients used by plant communities (Marschestner, 1995). Mg, Fe, and Ca, released by pyroxene weathering is linked to the atmospheric CO_2 content through carbonate mineral precipitation (Berner et al., 1983; Brady, 1991; Brady and Carroll, 1994; Berner, 1995; Gislason et al., 1996).

The variation of pyroxene/pyroxenoid dissolution rates with pH is enigmatic. In contrast with the dissolution rates of many silicate minerals including the alkali feldspars (Knauss and Wolery, 1986; Blum and Stillings, 1995), muscovite (Knauss and Wolery, 1989), and kaolinite (Nagy, 1995) which exhibit a pronounced minima with pH at near neutral conditions, the dissolution rates of diopside (Knauss et al., 1993) and wollastonite (Xie, 1994) decrease monotonically with increasing pH to pH = 12. Lartigue (1994) reported that augite dissolution rates at 25°C decreased with increasing pH to pH = 6 but were independent of pH in more basic conditions. Although few surface titration data are available for the pyroxenes, Brantley and Chen (1995) estimated, using the models of Parks (1967) and of Sverjensky (1994) that the pH of zero surface charge (pH_{zpc}) of the pyroxene/pyroxenoids range from 5.9 to 7.25. No correlation, therefore, is evident between pH_{zpc} and the pH minimum of pyroxenes/pyroxenoids dissolution rates. In an attempt to resolve this enigma, steady state enstatite dissolution rates have been measured as a function of pH, solution composition, and temperature. The purpose of the present communication is to report the results of this experimental study and use these results to deduce the dissolution mechanism of the pyroxene/pyroxenoid minerals.

A number of studies have characterized enstatite dissolution rates over the past several decades. Luce et al. (1972) reported an enstatite dissolution rate at 25°C and pH = 1.6. Schott et al. (1981) measured enstatite dissolution rates at 22°C at pH 1, 2, and 6, as well as 72°C and pH 6. Ferruzzi (1993) measured enstatite dissolution rates at 25°C and pH ranging from 2 to 7. Siegel and Pfannkuch (1984) generated an enstatite dissolution rate at 22°C and pH 4. A review of these data as well as those of other inosilicates are given by Brantley and Chen (1995). Oelkers (1999) presented a comparison of enstatite and forsterite dissolution rates and mechanisms; some of the data reported in this paper are illustrated in the figures presented in this previous work.

* Author to whom correspondence should be addressed (oelkers@lucid.ups-tlse.fr).

2. THEORETICAL BACKGROUND

The standard state adopted in this study is that of unit activity for pure minerals and H_2O at any temperature and pressure. For aqueous species other than H_2O, the standard state is unit activity of the species in a hypothetical 1 molal solution referenced to infinite dilution at any temperature and pressure. All aqueous activities and equilibrium constants used in the present study were generated using EQ3NR (Wolery, 1983) and SUPCRT92 (Johnson et al., 1992), respectively.

The overall rate of a chemical reaction (r) can be considered to be the difference between the forward rate (r_+) and the reverse rate (r_-) such that

$$r = r_+ - r_- = r_+\left(1 - \frac{r_-}{r_+}\right). \tag{1}$$

It has been demonstrated with the aid of transition state theory, that this second term, which accounts for the effects of inverse reaction can be expressed as (Aagaard and Helgeson, 1977; 1982; Lasaga, 1981; Helgeson et al., 1984; Murphy and Helgeson, 1987)

$$\left(1 - \frac{r_-}{r_+}\right) = (1 - \exp(-A/\sigma RT)), \tag{2}$$

where A refers to the chemical affinity of the overall reaction, σ stands for Temkin's average stoichiometric number equal to the ratio of the rate of destruction of the activated or precursor complex relative to the overall rate, R designates the gas constant, and T represents absolute temperature. All steady state dissolution rates reported in the present study were performed at far from equilibrium conditions, such that $A \gg \sigma RT$. At these conditions, (r_-/r_+) in Eqn. 1 tends to zero and the overall rate, r, is equal to r_+.

For the case of mineral dissolution reactions, r_+ is assumed to be proportional to the concentration of a rate controlling precursor complex at the mineral surface in accord with (see Wieland et al., 1988; Oelkers et al., 1994)

$$r_+ = k_+[P^\bullet], \tag{3}$$

where k_+ refers to a rate constant consistent with the $P^\bullet$ precursor complex and $[P^\bullet]$ stands for its concentration. The precursor complex is assumed to be in equilibrium with the dissolving mineral and therefore the variation of its concentration with aqueous solution composition can be deduced from the law of mass action for the reaction forming this complex. Taking into account the structures and dissolution rate variation with aqueous solution composition of a variety of minerals, Oelkers and Schott (1995b) and Oelkers (1996) concluded that two general types of reactions form rate controlling precursor complexes at mineral surfaces: (1) simple adsorption reactions and (2) metal–proton exchange reactions. Minerals whose dissolution rates are controlled by simple adsorption reactions include those whose dissolution requires the breaking of only one type of cation–oxygen bond. Examples of these minerals are single (hydr)oxides (e.g., gibbsite; Nagy and Lasaga, 1992, and quartz; Berger et al., 1994) and some multioxide silicates (e.g., anorthite; Oelkers and Schott, 1995a). Because their rate controlling precursor complexes are formed by simple adsorption reactions, the concentration of these complexes and thus the dissolution rate of these minerals at far from equilibrium conditions are independent of the aqueous concentration of the metals comprising the mineral. The variation of the overall dissolution rate of these minerals plotted as a function of its chemical affinity exhibits a characteristic dissolution plateau at far from equilibrium conditions ($A \gg \sigma RT$, Lasaga et al., 1994; Berger et al., 1994; Oelkers, 1996). Moreover, as the most common species involved in these precursor complex forming adsorption reactions are H^+ and OH^-, the variation of dissolution rates for these minerals typically minimize near their pH of zero surface charge.

Minerals whose rate controlling precursor complex is formed by metal–proton exchange reactions include those multi–oxides whose dissolution requires the breaking of several different cation–oxide bond types. For a wide variety of minerals these exchange reactions form neutrally charged precursor complexes (see Chou and Wollast, 1984; 1985; Sverdrup and Warfvinge, 1993; 1995; Schott and Oelkers, 1995; Oelkers, 1996; Oelkers and Schott, 1999). These exchange reactions invoke the breaking of the more reactive cation–oxygen bonds that are not essential to the structure, thus better exposing to hydrolysis the bonds essential to the structure. Examples of minerals following this type of reaction mechanism include albite (Chou and Wollast, 1984; 1985; Oelkers et al., 1994), K-feldspar (Gautier et al., 1994), kaolinite (Devidal, 1994; Devidal et al., 1997), kyanite (Oelkers and Schott, 1999), analcime (Murphy et al., 1996), and heulandite (Ragnarsdottir, 1993; Ragnarsdottir et al., 1996). For the case where the precursor complex is formed by the exchange of one type of metal cation, the precursor complex forming reaction can be expressed as

$$zn_4H^+ + >\text{M–OH} = P^\bullet + n_4\,M^{z+}, \tag{4}$$

where >M–OH represents a potentially reactive surface site, n_4 stands for a stoichiometric coefficient equal to the number of cations that need to be removed from the mineral structure to create one precursor complex, M denotes the exchanged metal, and z designates its valence. Taking account of the law of mass action for exchange reaction (4) and the fact that there are a limited number of total possible exchange sites on the mineral surface, an equation describing the forward dissolution rate of minerals that follow this mechanism can be expressed as (see Oelkers et al., 1994; Oelkers, 1996)

$$r_+ = k_+[P^\bullet] = k_+\left(\frac{K_4^\bullet\left(\frac{a_{H^+}^z}{a_{M^{z+}}}\right)^{n_4}}{1 + K_4^\bullet\left(\frac{a_{H^+}^z}{a_{M^{z+}}}\right)^{n_4}}\right), \tag{5}$$

where $K_4^\bullet$ designates the equilibrium constant for reaction (4) and a_i denotes the activity of the subscripted aqueous species. There are two major differences between adsorption and exchange reactions in terms of the overall dissolution mechanism. First, precursor forming exchange reactions break some of the weaker metal–oxygen bonds in the mineral structure liberating some cations. Second, because they liberate metals from the original mineral prior to the formation of the rate controlling complex, these exchange reactions result in overall dissolution

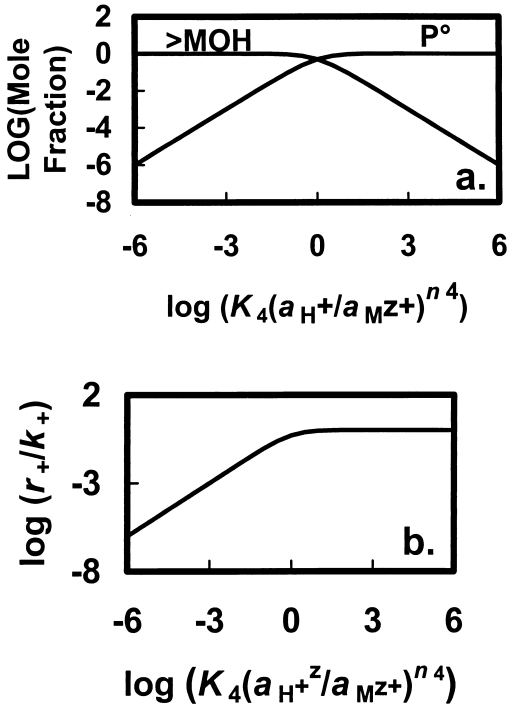

Fig. 1. Computed variation of the (a) the surface speciation and (b) logarithm of dissolution rates as a function of $K_4^*(a_{H^+}^z/a_{M^{z+}})^{n_4}$. The curves in these figures were generated from Eqn. 5 and the law of mass action for reaction (4).

rates that decrease with the aqueous activity of the exchanged metal.

Equation 5 prescribes the variation of dissolution rates as a function of solution composition; surface speciation and dissolution rates consistent with Eqn. 5 are illustrated in Figure 1. When $K_4^*(a_{H^+}^z/a_{M^{z+}})^{n_4}$ is significantly less than 1, there is a significant concentration of the metal M at the mineral surface, the relative number of surface precursor complexes is low, and the dissolution rate will depend on both pH and aqueous M^{z+} activity consistent with

$$r_+ = k_+ K_4^* \left(\frac{a_{H^+}^z}{a_{M^{z+}}}\right)^{n_4}. \tag{6}$$

In contrast, when $K_4^*(a_{H^+}^z/a_{M^{z+}})^{n_4}$ is substantially greater than 1, essentially all of M is removed from the mineral surface, the surface precursor complex concentration maximizes, and dissolution rates become independent of pH and the aqueous M^{z+} activity ($r_+ = k_+$). The thickness of the M depleted leached layer is controlled by the relative rates of metal and proton diffusion into and out of the leached layer, respectively, versus that of the surface reaction controlled breaking of the mineral structure (Doremus, 1975). Although values of K_4^* are not yet available for metal exchange reactions on mineral surfaces, it clearly plays a role in mineral dissolution kinetics. As the activity ratio $(a_{H^+}^z/a_{M^{z+}})^{n_4}$ increases with decreasing pH and dissolved metal concentration, it will be relatively high in acidic solutions. It is at such conditions that substantial leached layer formation is commonly observed (cf. Schott et al., 1981).

In cases where the metal is not completely depleted from the mineral surface, $K_4^*(a_{H^+}^z/a_{M^{z+}})^{n_4} < 1$, the pH variation of far from equilibrium dissolution rates (r_+) are controlled by the stoichiometry of the precursor complex and aqueous speciation of the exchanged metal, M. For example, in the absence of other complexing ligands, the exchanged metal will form hydroxide complexes according to

$$M^{z+} + yH_2O = M(OH)_y^{(z-y)+} + yH^+, \tag{7}$$

where y designates the stoichiometric number of hydroxide ions in each aqueous metal hydroxide complex for which the law of mass action is given by

$$K_{7,y} = \frac{a_{M(OH)_y^{z-y}} a_{H^+}^y}{a_{M^{z+}}}, \tag{8}$$

where $K_{7,y}$ stands for the equilibrium constant for the yth hydrolysis reaction represented by reaction (7). The total concentration of the metal M in solution ($C_{tot,M}$) is given by

$$C_{tot,M} = C_{M^{z+}} + \sum_{y=1}^{y'} C_{M(OH)_y^{(z-y)+}} = \frac{a_{M^{z+}}}{\gamma_{M^{z+}}} + \sum_{y=1}^{y'} \frac{a_{M(OH)_y^{(z-y)+}}}{\gamma_{M(OH)_y^{(z-y)+}}}, \tag{9}$$

where γ_i stands for the activity coefficient of the subscripted species and y' designates the total number of possible hydroxide complexes. Combining Eqns. 8 and 9 and rearranging yields

$$a_{M^{z+}} = C_{tot,M}\left[\frac{1}{\gamma_{M^{z+}}} + \sum_{y=1}^{y'} \frac{K_{7,y}}{a_{H^+}^y \gamma_{M(OH)_y^{(z-y)+}}}\right]^{-1} \tag{10}$$

which when combined with Eqn. 6 leads to

$$r_+ = \frac{k_+ K_4^*}{C_{tot,M}^{n_4}}\left(\frac{a_{H^+}^z}{\gamma_{M^{z+}}} + \sum_{y=1}^{y'} \frac{a_{H^+}^{z-y} K_{7,y}}{\gamma_{M(OH)_y^{(z-y)+}}}\right)^{n_4}. \tag{11}$$

For a series of experiments performed at constant ionic strength, activity coefficients are essentially pH independent. Thus it follows from Eqn. 11 that at a constant ionic strength and total aqueous M concentration, the pH variation of a mineral's dissolution rate is controlled by the magnitude of the equilibrium constants for the hydrolysis constants for the metal M and the stoichiometric coefficient n_4. Although Eqn. 11 appears to prescribe a complicated behavior, the pH variation of log r_+ is in fact directly proportional to the pH variation of the logarithm of the corresponding metal oxide (or oxy-hydroxide) solubility. This can be demonstrated by considering the dissolution reaction of the metal oxide $MO_{z/2}$ represented by

$$MO_{z/2} + zH^+ = M^{z+} + \frac{z}{2} H_2O \tag{12}$$

for which the law of mass action is given by

$$K_{12} = \frac{a_{M^{z+}}}{a_{H^+}^z}, \tag{13}$$

where K_{12} represents the equilibrium constant of reaction (12). Combining Eqns. 10 and 13 yields

Table 1. Chemical composition of Bramble Enstatite as determined by electron microprobe. Values are the average of 5 measurements.

Element	Atomic percent
Na	0.01
K	0
Ca	0.088
Si	20.03
Al	0.054
Mg	16.996
Mn	0.01
Fe	2.718
Ni	0.01
Ti	0.004
Cr	0.004
O	60.046

$$C^*_{\mathrm{tot,M}} = K_{12}\left(\frac{a^z_{\mathrm{H}^+}}{\gamma_{\mathrm{M}^{z+}}} + \sum_{y=1}^{y'} \frac{a^{(z-y)}_{\mathrm{H}^+} K_{7,y}}{\gamma_{\mathrm{M(OH)}_y^{(z-y)+}}}\right), \qquad (14)$$

where $C^*_{\mathrm{tot,M}}$ designates the aqueous concentration of the metal M is equilibrium with $MO_{z/2}$. Comparison of Eqns. 11 and 14 demonstrates that log r_+ is directly proportional to the log of $MO_{z/2}$ solubility; the relative magnitude of their variations with pH is given by the stoichiometric coefficient n_4. This proportionality is apparent by comparing the dissolution rates of the aluminosilicates albite, K-feldspar, muscovite, or kyanite with the solubility of gibbsite, diaspore, or corundum. It should be noted, however, that the variation of r_+ with pH itself is frequently a crude tool for distinguishing the identity of the precursor forming reaction. This is because stability constants of surface complexes often mimic the corresponding metal hydrolysis constants (Schlinder and Stumm, 1987). Consequently, the absolute value of a mineral's surface charge often has a similar pH dependence as the solubility of one of its constituent metal oxides. This is the case for the aluminosilicates; the absolute value of their surface charge has a similar pH dependence to the solubility of aluminum oxide phases. It is, however, not the case for the pyroxenes/pyroxenoids enstatite, diopside, or wollastonite which likely have a $pH_{zpc} \sim 6$ (see above), whereas Mg, Ca, and Si hydroxide complex formation is negligible at pH < 9.

3. MATERIAL PREPARATION AND EXPERIMENTAL METHODS

Natural enstatite crystals from Bramble, Norway, having an average size of ~0.5 cm were obtained from Wards Natural Science. X-ray diffraction (XRD) of this material indicated the presence of substantial quantities of talc. These crystals were hand picked to remove talc, then ground with an agate mortar and pestle. The remaining talc was eliminated by density separation using CH_3Br. The size fraction between 50 and 100 μm was obtained by sieving. This fraction was cleaned ultrasonically using acetone to remove fine particles, rinsed with distilled water, and dried overnight at 80°C. XRD of the resulting powder confirmed the removal of all but minor quantities of talc. The fact that essentially all talc was removed from this solid is supported by (1) the low specific surface area of the resulting powder, and (2) the observation that the enstatite steady state dissolution rates measured in the present study is stoichiometric (see below). The specific surface area of the cleaned powder was 800 $\pm$ 80 cm^2/g as determined by krypton adsorption using the B.E.T. method. The chemical composition of the enstatite, determined by electron microprobe is given in Table 1. The data presented in this table indicates this enstatite contains substantial iron, having an average composition of $(Mg_{0.849}Fe_{0.136}Ca_{0.004})Si_{1.002}O_3$ when normalized to 3 oxygens.

All dissolution experiments were performed in mixed flow reactors. The first experimental series was carried out in a titanium mixed flow reactor system similar to that described in detail by Berger et al. (1994). The inlet fluid was injected into the reactor through a 10 μm filter via a Milton Roy high pressure liquid chromatography pump that allows flow rates ranging from 1 to 10 g/min. Enstatite dissolution occurred in a 215 ml Parr pressurized reactor vessel, which was continuously stirred with a Parr magnetically driven stirrer and kept at a constant temperature $\pm$1°C by a Parr controlled furnace. The reactive fluid left the reactor through the 10 μm titanium filter, whereupon it was quenched, and passed through a back pressure regulator. All parts in contact with the high temperature reactive fluid are made of titanium. All other dissolution experiments were performed in 250 ml Azlon plastic beakers continuously stirred with floating Teflon stirring bars. These reactors were immersed in a water bath held at a constant temperature $\pm$1°C. Fluid was injected into this reactor using a Gilson peristaltic pump, which allows fluid flow rates from 0.01 to 10 g/min. The solution left the reactor through a 0.45 μm Teflon filter. No additional filtering was performed on outlet fluid sampled obtained from either reactor prior to chemical analysis. The inlet fluid during all experiments was stored in compressible, sealed polyethylene containers.

Each experimental series consisted of a sequence of experiments performed on a single enstatite powder in a single reactor. At the onset of each experimental series, the powder and a quantity of initial inlet fluid were introduced to the reactor. The reactor was heated to the desired temperature and the inlet fluid was passed through the reactor at a constant flow rate until the outlet solution attained a steady state Mg and Si concentration. Steady state outlet concentrations were obtained after an elapsed time ranging from 2 hours to 4 days, depending on the flow rate. After this steady state was verified with a minimum of three constant Mg and Si concentration outlet fluid samples taken obtained over several residence times (the residence time is defined as the volume of the reactor divided by the reactive fluid flow rate), the temperature, inlet fluid composition, and/or fluid flow rate were changed to the next desired experimental condition. Dissolution experiments were carried out in fluids comprised of demineralized/degassed H_2O, Merck reagent grade HCl, NaOH, NH_4Cl, NH_4OH, and $MgCl_2$, and H_4SiO_4 obtained by the dissolution of amorphous silica for one week at 90°C. All inlet fluids other than those for experiments En4–13 and En4–17 had stoichiometric ionic strengths of 0.01 mol/kg; those for experiments En4–13 and En4–17 were somewhat higher to enable attainment of pH < 2. Magnesium compositions of the inlet and outlet fluids were determined using atomic adsorption spectroscopy (Perkin Elmer Zeeman 5000); silica compositions were measured using the Molbyldate Blue method (Koroleff, 1976). The reproducibility of chemical analyses were $\pm$4% for Si and Mg concentrations greater than 0.5 and 0.1 ppm, respectively, but on the order of $\pm$10% at lower concentrations. Outlet fluid pH was measured at 25°C immediately after sampling. pH values at the elevated experimental temperatures were computed using EQ3NR (Wolery, 1983). Outlet solutions were undersaturated with respect to all possible secondary phases other than for the solutions having pH > 9, which were slightly supersaturated with respect to antigorite and chrysotile, and likely supersaturated with respect to magnesite. There was, however, no evidence of any secondary phase precipitation during the experiments.

4. EXPERIMENTAL RESULTS

Two examples of the approach of reactive fluid compositions to steady state are illustrated in Figure 2. It can be seen in this figure that the initial dissolution of enstatite was nonstoichiometric; Mg was initially released faster than Si at pH 2 whereas Si was initially released faster than Mg at pH 10.7. Stoichiometric dissolution was observed once steady state was reached. The direction of this preferential release is consistent with the stoichiometry of a magnesium for proton exchange reaction, such as reaction (4), which favors a surface that is enriched in Mg at basic relative to acidic conditions. A similar behavior has

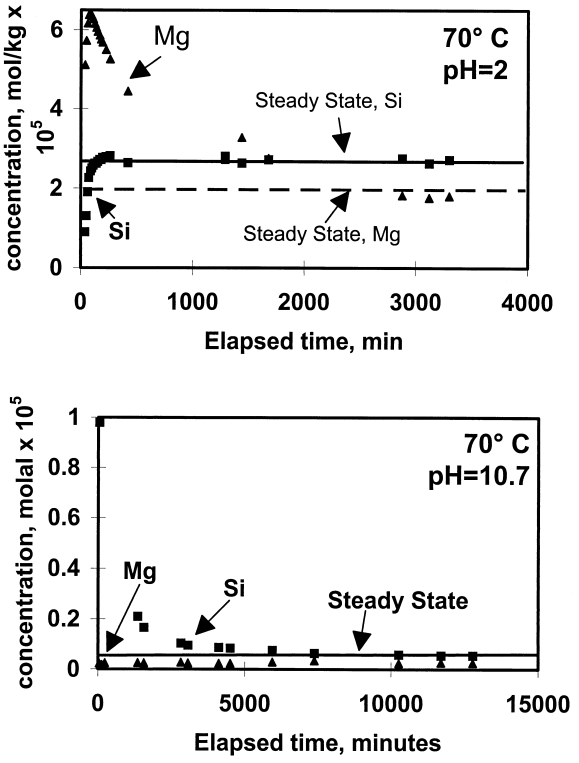

Fig. 2. Temporal evolution of the reactive fluid Mg and Si concentration during experiments (a) En5–15, and (b) En6–17. The filled squares and triangles represent measured Si and Mg concentrations, respectively, whereas the linear curves correspond to the attained steady state concentrations.

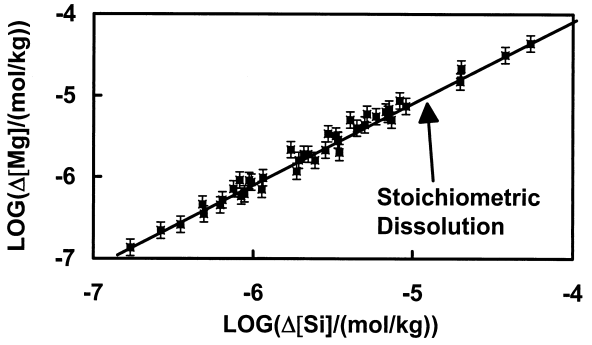

Fig. 3. The logarithm of the difference between inlet and outlet solution Mg concentration as a function of the corresponding logarithm of the difference between inlet and outlet solution Si concentration. The symbols represent measured solution compositions; the error bars surrounding these points correspond to a 4% uncertainty in Δ[Mg] and Δ[Si]. The solid line corresponds to the Mg/Si ratio of the dissolving enstatite.

previously been observed for forsterite. Oelkers (2001) reported a preferential initial Mg release at pH 2. Pokrovsky and Schott (2000) observed a preferential initial Mg release at pH 2 but a preferential initial Si release at pH 12. Chen and Brantley (1998) also noted a preferential initial release of alkaline earth elements during diopside and anthophyllite dissolution experiments. As dissolution rates tend to be relatively slow for these silicates at high pH, it may take substantial time to reach stoichiometric steady state dissolution during laboratory dissolution experiments. Failure to wait sufficient time could lead to ambiguities in the presumed pH dependencies of mineral dissolution rates.

The difference between inlet and outlet Mg concentration for all steady state experiments is depicted as a function of the corresponding change in Si concentration in Figure 3. The solid line in this figure corresponds to the Mg/Si ratio of the dissolving enstatite. It can be seen in this figure that within analytical uncertainty, steady state enstatite dissolution was stoichiometric.

Steady state dissolution rates (r) were computed from measured steady state solution compositions using

$$r = \frac{\Delta m_i F}{\nu_i s}, \tag{15}$$

where Δm_i stands for the concentration difference between the inlet and outlet of the ith element in solution, F represents the fluid flow rate, ν_i refers to the stoichiometric number of moles of the ith element in one mole of enstatite, and s denotes the total mineral surface area present in the reactor. Resulting dissolution rates, together with inlet and outlet total magnesium and silica concentrations, and computed solution pH and chemical affinities for all experiments are listed in Tables 2–4. The surface areas used to calculate these rates were those measured from krypton adsorption using the B.E.T. method on the fresh (unreacted) mineral powder. Rates reported in this study are, therefore, given in units of mass of enstatite dissolved per cm^2 of initial enstatite surface area per second. To assess the potential affects of surface area evolution during the experiments on computed dissolution rates, at least one set of experimental conditions (solution composition, fluid flow rate, temperature) was repeated during each experimental series. The repeated runs produced rates that were within ~10% of those originally measured. For example, in experimental series En1, experiments En1–3, En1–15 and En1–26 were performed on a single powder at essentially identical conditions. Measured steady state rates were 5.1, 4.7, and 4.7 $\times$ 10^{13} (mol of enstatite)/cm^2/s, respectively, for these three experiments. This observation indicates that either (1) the total enstatite surface area remained essentially constant during the experiments or (2) any additional surface area resulting from dissolution was unreactive (e.g., Gautier et al., 2001). Chemical affinity values listed in Tables 2–4 are consistent with enstatite dissolution represented by

$$MgSiO_3 + 2H^+ \Leftrightarrow Mg^{+2} + SiO_2(aq) + H_2O \tag{16}$$

and were calculated using

$$A = RT \ln\left(\frac{K_{16} a_{H^+}^2}{a_{Mg^{+2}} a_{SiO_2(aq)}}\right) \tag{17}$$

where K_{16} stands for the equilibrium constant of reaction (16), and a_i represents the activity of the subscripted aqueous species. No attempt was made to estimate A for the exact composition of the enstatite used in the experiments.

Measured steady state enstatite dissolution rates at 70°C are illustrated as a function of aqueous Si and Mg activity in Figure

Table 2. Experimentally measured enstatite forward dissolution rates at 70°C and pH = 2.

Sample number	Surface area (cm^2)[a]	Fluid flow rate (gm/min)	Inlet Si conc.[b]	Inlet Mg conc.[b]	Outlet Si conc.[b]	Outlet Mg conc.[b]	r_+[c]	A[d]
En1–3	2135	1.98	0	0	3.30	3.19	5.10	22.77
En1–6	2135	9.67	0	0	0.75	0.71	5.66	24.86
En1–8	2135	0.95	0	0	5.90	5.55	4.38	21.97
En1–10	2135	1.08	0	200	3.47	202	2.93	19.88
En1–12	2135	2.01	0	200	1.95	197	3.06	20.30
En1–13	2135	9.77	0	200	0.40	206	3.05	21.38
En1–15	2135	2.04	0	0	2.95	3.4	4.70	22.80
En1–17	2135	2.08	0	1000	1.56	988	2.53	19.49
En1–19	2135	1.21	0	1000	2.45	1014	2.31	19.12
En1–21	2135	1.14	0	5000	2.14	5187	1.90	18.29
En1–23	2135	2.00	0	5000	1.05	5053	1.64	18.80
En1–26	2135	2.14	0	0	2.84	2.94	4.74	22.95
En2–3	1791	0.81	0	0	7.38	5.03	5.56	21.88
En2–5	1791	0.23	0	0	19.80	14.9	4.24	20.43
En2–8	1791	1.23	0	0	4.06	5.03	4.65	22.30
En2–9	1791	1.81	0	0	2.21	1.90	3.72	23.41
En2–13	1791	0.68	0	200	4.47	204	2.83	19.69
En2–16	1791	0.68	8.2	0	15.20	5.94	4.43	21.26
En2–17	1791	2.52	8.2	0	9.92	2.16	4.03	22.27
En2–18	1791	0.65	0	0	7.12	6.87	4.31	21.69
En3–4	619	2.08	0	0	0.94	0.90	5.26	24.54
En3–6	619	4.13	0	0	0.48	0.46	5.34	25.48
En3–9	619	1.04	0	0	1.93	1.60	5.40	23.63
En3–11	619	2.03	0	0	0.82	0.91	4.48	24.62
En4–18	1503	1.02	18.5	0	22.5	3.42	4.51	21.37
En4–20	1503	2.11	18.5	0	19.4	2.21	5.85	21.78
En4–22	1503	0.61	18.5	0	24.4	4.99	3.99	21.05
En4–26	1503	0.67	0	0	5.18	5.95	3.85	22.01
En5–15	1935	1.98	0	0	2.53	1.91	4.31	23.43

[a] The surface areas in this table are equal to the product of the initial enstatite powder mass and the mass normalized B.E.T. surface area of this initial powder.
[b] mol/kg $\times 10^5$.
[c] (mol of enstatite)/cm^2/s $\times 10^{13}$ based on the difference between the inlet and outlet aqueous Si concentration for experiments other than En2–16, En2–17, En4–18, En4–20, and En4–22, which were based on aqueous Mg concentration.
[d] kcal/mol.

4. These rates exhibit a scattered behavior as a function of aqueous silica activity in Figure 4a. In contrast, these data appear to decrease systematically with increasing aqueous Mg activity as illustrated in Figure 4b. The solid curve in Figure 4b, which represents a least squares fit of the experimental data, has a slope equal to -0.123 with 95% confidence limits of ± 0.02. The coefficient of determination (R^2) of this fit of the data is 0.874. It can be seen that this curve provides a good description of the experimental data at all aqueous Si concentrations.

Measured steady state enstatite dissolution rates at 70°C at pH from 1 to 11 are illustrated in Figure 5. These measured rates decrease monotonically with increasing pH. The linear curve in the figure represents a least squares fit of the data. This curve has a slope of -0.206 with 95% confidence limits of ± 0.05. The coefficient of determination (R^2, Rosenthal and Rosnow, 1984) of this data fit is 0.927.

To within experimental uncertainty, the variation of measured constant temperature enstatite dissolution rates with aqueous magnesium activity is equal to the reciprocal square root of its dependence on aqueous hydrogen activity. This

Table 3. Experimentally measured enstatite forward dissolution rates at pH = 2 and temperatures other than 70°C (see Table 2).

Sample number	Surface area (cm^2)	Fluid flow rate (gm/min)	Temperature (°C)	Outlet Si conc.[a]	Outlet Mg conc.[a]	r_+[b]	A[c]
En1–27	2135	2.06	95	8.30	8.71	13.35	21.42
En1–28	2135	2.06	120	20.1	21.5	32.32	20.04
En1–29	2135	2.02	148	37.8	31.5	59.61	19.10
En1–30	2135	2.09	168	54.3	43.8	88.59	18.40
En2–12	1791	0.68	43	0.84	0.58	0.53	24.55
En2–19	1791	0.14	28	2.10	1.42	0.27	23.26

[a] mol/kg $\times 10^5$.
[b] (mol of enstatite)/cm^2/s $\times 10^{13}$.
[c] kcal/mol.

Table 4. Experimentally measured enstatite forward dissolution rates at 70°C and pH other than 2. Stoichiometric ionic strength of all inlet solutions other than En4–13 and En4–17 was 0.01 mol/kg (see Table 2).

Sample number	Inlet soln. composition	Surface area (cm^2)	Fluid flow rate (gm/min)	pH measured at 25°C	pH computed at 70°C	Outlet Si conc.[a]	Outlet Mg conc.[a]	r_+[b]	A[c]
En4–6	HCl + NH_4Cl	1503	0.68	2.52	2.52	3.39	2.86	2.56	21.15
En4–10	HCl + NH_4Cl	1503	0.75	2.99	2.99	2.44	1.60	2.03	20.29
En4–13	HCl	1503	0.73	1.03	1.03	9.08	7.43	7.35	24.85
En4–17	HCl	1503	0.70	1.51	1.51	6.79	6.34	5.27	23.46
En5–23	HCl + NH_4Cl	1935	1.00	3.00	3.00	3.40	2.83	2.92	19.64
En5–24	HCl + NH_4Cl	1935	0.50	3.04	3.04	5.01	4.39	2.14	18.95
En5–25	HCl + NH_4Cl	1935	0.99	3.65	3.65	1.87	1.17	1.60	18.61
En5–26	HCl + NH_4Cl	1935	0.99	4.07	4.07	1.13	0.70	0.97	17.99
En5–27	NH_4Cl	1935	1.00	5.80	5.13	0.49	0.35	0.42	15.71
En5–28	NH_4Cl	1935	0.65	5.96	5.17	0.64	0.52	0.36	15.12
En5–29	NH_4Cl + NH_4OH	1935	0.99	7.47	6.29	0.62	0.45	0.53	11.71
En5–30	NH_4Cl + NH_4OH	1935	0.49	7.54	6.36	0.97	0.86	0.41	10.74
En6–17	NaOH	3693	0.69	12.00	10.81	0.18	0.14	0.06	2.51
En6–20	NH_4OH	3693	0.69	10.77	9.58	0.26	0.22	0.08	2.73
En6–25	NH_4Cl + NH_4OH	3693	0.69	10.38	9.17	0.35	0.26	0.11	3.66
En6–30	NH_4Cl + NH_4OH	3693	0.68	9.09	7.91	1.15	0.97	0.35	5.66
En6–31	NH_4Cl + NH_4OH	3693	0.68	7.95	6.77	2.08	1.90	0.64	8.32
En6–32	NH_4Cl + NH_4OH	3693	1.71	7.97	6.79	0.88	0.62	0.68	9.68

[a] mol/kg $\times 10^5$.
[b] (mol of enstatite)/cm^2/s $\times 10^{13}$.
[c] kcal/mol.

observation is consistent with the formation of neutrally charged rate controlling precursor complexes through the exchange of two protons for one Mg near the enstatite surface, consistent with reaction (4). These experimental data indicate that enstatite dissolution is consistent with Eqn. 6, where M^{z+} corresponds to Mg^{2+}. The value of the stoichiometric coefficient n_4 can be deduced with the aid of Figure 6, which illustrates the logarithm of enstatite dissolution rates as a function of log $(a^2_{H^+}/a_{Mg^{2+}})$. The linear curve in this figure represents a linear least squares fit of the data. This linear curve has a slope of 0.117 with a 95% confidence limit of ± 0.02. It follows that the enstatite dissolution rates measured in the present study are all consistent with

$$r_{+,\text{enstatite}} = k_+ \left(\frac{a^2_{H^+}}{a_{Mg^{2+}}} \right)^{1/8}, \tag{18}$$

where $r_{+,\text{enstatite}}$ designates the forward (far from equilibrium) enstatite dissolution rate. As emphasized above, Eqn. 18 implies that the pH variation of log $r_{+,\text{enstatite}}$ will be equal to one-eighth of the corresponding pH variation of either periclase (MgO) or brucite ($Mg(OH)_2$) solubility.

The variation of mineral dissolution rates with temperature is commonly described using a form of the empirical Arrhenius equation. The constant temperature dissolution rates of many minerals, including enstatite, depend on pH and solution composition. To overcome possible ambiguities of these effects, in the present study, the empirical Arrhenius equation will be applied to rates at constant pH and solution composition in accord with

$$r_{+\text{pH},C_i} = A_A \exp\left(\frac{-E_A}{RT} \right), \tag{19a}$$

where $r_{+\text{pH},C_i}$ stands for the forward dissolution rate at con-

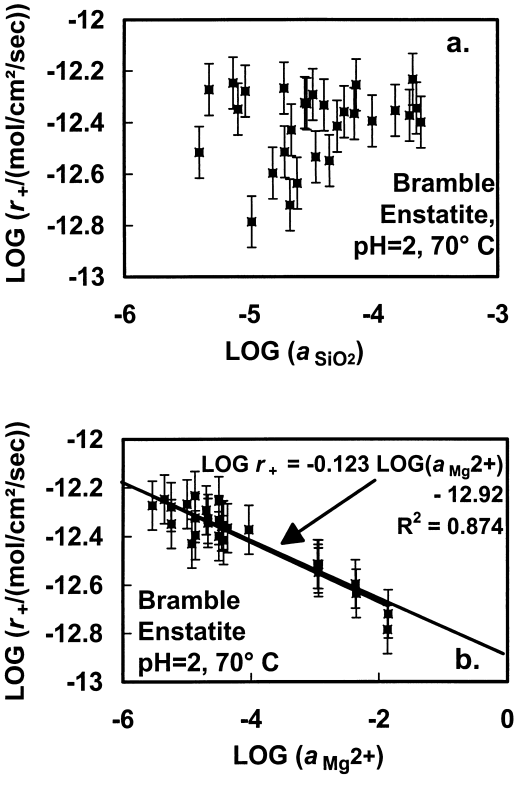

Fig. 4. Variation of the logarithm of steady state enstatite dissolution rates at pH = 2 and 70°C with the logarithm of aqueous (a) silicon and (b) magnesium activity. The symbols correspond to experimental data reported in Table 2, and the error bars correspond to a ± 0.1 log unit uncertainty, which is consistent with the $\sim \pm 20\%$ uncertainty estimated for these data. The linear curve in (b) represents a least squares fit of the data; the equation and coefficient of determination (R^2) of this curve are given in the figure.

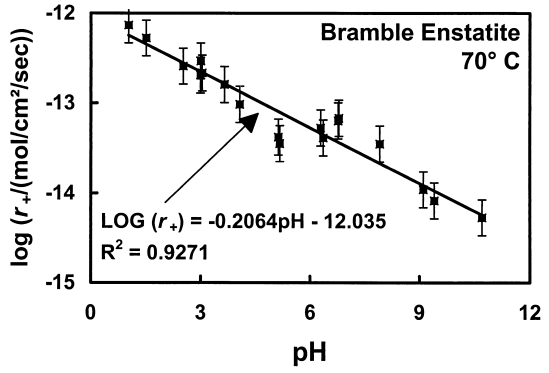

Fig. 5. Variation of the logarithm of steady state enstatite dissolution rates with pH. The symbols correspond to experimental data obtained in the present study and the error bars correspond to a ±0.1 log unit uncertainty, which is consistent with the ~±20% uncertainty estimated for these data. The linear curve represents a least squares fit of the data; the equation and coefficient of determination (R^2) of this curve are given in the figure.

stant pH and solution composition, A_A designates a pre-exponential factor, and E_A refers to the activation energy defined by

$$E_A = -2.303R\left(\frac{\partial \log r_+}{\partial\left(\frac{1}{T}\right)}\right)_{\mathrm{pH},C_i} . \qquad (19b)$$

An Arrhenius plot depicting the logarithm of enstatite dissolution rates as a function of reciprocal temperature is illustrated in Figure 7. The filled symbols correspond to the measured rates, whereas the open symbols correspond to rates normalized to $(a^2_{H^+}/a_{Mg^{2+}}) = 0.1$. Taking account of Eqn. 19b, it follows that the slopes of the line, corresponding to a fit of the open symbols, is equal to $-E_A/2303R$. The straight line depicted in this figure corresponds to an activation energy of 48.5 kJ/mol for the data obtained in this study at pH 2. This activation energy is essentially equal to that reported by Schott et al.

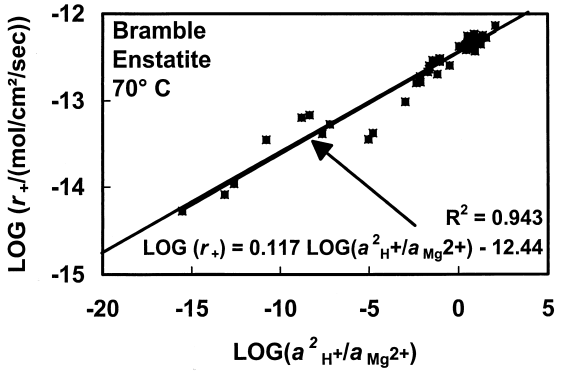

Fig. 6. Logarithms of steady state enstatite dissolution rates as a function of the logarithm of the activity ratio ($a^2_{H^+}/a_{Mg^{2+}}$). The symbols represent measurements performed in the present study at 70°C, whereas the linear curve corresponds to a least squares fit of the data; the equation and coefficient of determination (R^2) of this curve are given in the figure.

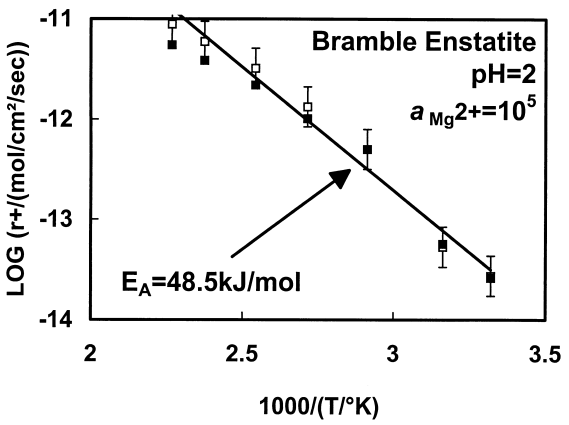

Fig. 7. Variation of the logarithm of steady state enstatite dissolution rates as a function of 1000 times reciprocal temperature at pH = 2. The filled and open symbols correspond to the measured rates and measured rates normalized to a constant Mg^{2+} activity of 10^{-5}, respectively; the error bars correspond to a ±0.1 log unit uncertainty, which is consistent with the ~±20% uncertainty estimated for these data. The linear curve corresponds to a least squares fit of the open symbols.

(1981) from experiments performed at pH 6. Combining Eqn. 18 and 19a leads to

$$r_{+,\mathrm{enstatite}} = A_A \exp(-E_A/RT)\left(\frac{a^2_{H^+}}{a_{Mg^{2+}}}\right)^{1/8} \qquad (20)$$

which allows description of forward enstatite dissolution rates as a function of both solution composition and temperature. Regression of the data obtained in the present study yields $A_A = 2.4 \times 10^{-4}$ (mol of enstatite)/cm^2/s.

5. DISCUSSION

The observed variation of enstatite dissolution rates with solution composition stems from the structure and dissolution mechanism of this pyroxene. The pyroxene structure consists of chains of corner sharing silicon tetrahedra; these chains are linked together by divalent cations. There are two distinct cation sites, commonly referred to as the M_1 and M_2 sites; M_1 sites are found between the apices and M_2 sites are found between the bases of the silica tetrahedra chains. The early period of pyroxene dissolution is nonstoichiometric. At acidic conditions, the M_2 cations are released preferentially relative to both silica and the cation on the M_1 sites; with continued reaction, the rate of cation release from the M_2 sites decreases and, after reaching a steady state, all species are released in stoichiometric proportions (Schott et al., 1981; see also the discussion of Murphy and Helgeson, 1987; 1989). This preferential release of cations from the M_2 sites in pyroxenes are caused by H^+ exchange reactions (Schott et al., 1981; Schott and Berner, 1985; Murphy and Helgeson, 1987). The preferential release of divalent cations from the M_2 sites in acidic solutions is consistent with the formation of leached layers on the surfaces of dissolved pyroxenes and wollastonite, which is most apparent at low pH (Luce et al., 1972; Schott et al., 1981; Berner and Schott, 1982; Schott and Berner, 1983; 1985; Petit et al., 1987; Schott and Petit, 1987; Peck et al., 1988; Ferruzzi,

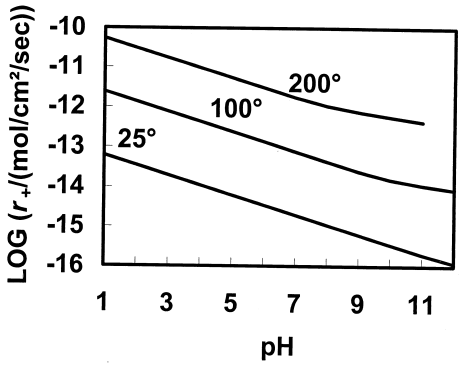

Fig. 8. Logarithms of enstatite forward dissolution rates as a function of pH for solutions in the system MgO–SiO_2–H_2O–HCl–NaCl with a total Mg concentration of 10^{-4} mol/kg and an ionic strength of 0.1 mol/kg. The curves correspond to the temperatures given in the figure—see text.

1993; Casey et al., 1993). Schott et al. (1981) also observed a concurrence of x-ray photoelectron spectroscopy (XPS) band positions in fresh and acid leached enstatite, indicating that H^+ replaces Mg in the enstatite structure during hydrolysis without rearranging the silica bonding network. The breaking of metal–oxygen bonds via this exchange reaction will not destroy the mineral structure but will only serve to partially liberate the silica tetrahedral chains leaving them more assessable to attack by other aqueous species. The breaking of the Si–O–Si linkages within the tetrahedral chains is relatively slow, and completes the dissolution process. Within the framework of transition state theory, rates are proportional to the concentration of the surface precursor complex, which in this case is partially detached silica tetrahedra near the enstatite surface. Because this precursor complex is formed from proton/magnesium exchange reactions, constant temperature enstatite forward dissolution rates are independent of aqueous Si activity, but increase with decreasing pH and aqueous Mg^{2+} activity, consistent with Eqn. 18.

Predicted enstatite forward dissolution rates are illustrated in Figure 8 and tabulated in Table 5 as a function of pH and temperature for solutions in the system MgO–SiO_2–H_2O–HCl at $C_{\text{tot,Mg}} = 10^{-4}$ mol/kg. The values in this figure and table were generated with Eqn. 20 together with $E_A = 48.5$ kJ/mol, $A_A = 2.4 \times 10^{-4}$ (mol of enstatite)/cm^2/s, and aqueous activities generated using the EQ3NR computer code (Wolery, 1983). Predicted enstatite forward dissolution rates decrease monotonically with increasing pH. The curve corresponding to rates at 25°C is linear with a slope of -0.25 at pH < 12. This behavior is due to lack of substantial aqueous Mg–hydroxide complexing at these conditions. The slope becomes shallower at higher pH due to the formation of $Mg(OH)^+$ which lowers the aqueous activity of Mg^{2+}. This effect occurs at lower pH at elevated temperature due to the increase stability of $Mg(OH)^+$ at these conditions. Note that the predictions presented in Fig. 8 and Table 5 are based on the assumption that activation energy for enstatite dissolution is pH and temperature independent for constant $a_{Mg^{2+}}$. In contrast, Chen and Brantley (1998) argued, based on their experimental work, that the activation energy of pyroxene dissolution depends on pH. It should be emphasized in this regard, that because activities of dissolved

Table 5. Predicted values of the enstatite steady state forward dissolution rate as a function of temperature and pH for solutions in the system MgO–SiO_2–H_2O–HCl at $C_{\text{tot,Mg}} = 10^{-4}$ mol/kg. All values in this table were generated with Eqn. 20 together with $E_A = 48.5$ kJ/mol, $A_A = 2.4 \times 10^{-4}$ (mol of enstatite)/cm^2/s, and aqueous activities generated using the EQ3NR computer code (Wolery, 1983) (see text).

	Temperature °C					
pH	25	50	100	150	200	300
1	−13.21	−12.60	−11.62	−10.86	−10.27	−9.39
2	−13.46	−12.85	−11.87	−11.11	−10.52	−9.64
3	−13.71	−13.10	−12.12	−11.36	−10.77	−9.89
4	−13.96	−13.35	−12.37	−11.61	−11.02	−10.14
5	−14.21	−13.60	−12.62	−11.86	−11.27	−10.37
6	−14.46	−13.85	−12.87	−12.11	−11.51	−10.61
7	−14.71	−14.10	−13.12	−12.36	−11.76	−10.85
8	−14.96	−14.35	−13.37	−12.59	−11.97	−11.00
9	−15.21	−14.60	−13.61	−12.80	−12.12	−11.10
10	−15.46	−14.83	−13.81	−12.99	−12.24	−11.22
11	−15.70	−15.06	−13.95	−13.11	−12.36	−11.22
12	−15.92	−15.22				
13	−16.08					

metals are not generally held constant during experimental dissolution studies performed as a function of temperature and pH, it is not possible to determine directly the extent to which aqueous activity independent activation energies depend on pH from these data.

The variation with pH of a wide variety of pyroxene/pyroxenoid forward dissolution rates are illustrated in Figure 9. As previously observed by Brantley and Chen (1995), the forward dissolution rates of all pyroxene/pyroxenoid minerals decrease monotonically with pH. For the case of diopside and wollastonite these rates decrease with increasing pH until at least pH = 12. No minimum is observed although these minerals have a pH_{zpc} of ~7 (see above and Sverjensky, 1994; Brantley and Chen, 1995). The curves in Figure 9 represent a linear least squares regression of each data set. A summary of these regression results are given in Table 6. The slopes indicated in Figure 9 and Table 6 are those obtained by least squares fit in the present study and may, therefore, differ somewhat from those reported in the original sources. The uncertainty limits given in Table 6 correspond to 95% confidence limits of each data set. Some of the scatter apparent in Figure 9 may originate from the fact that the aqueous activity of divalent cations was not held constant in the experiments. Nevertheless, a survey of these regression results and others listed in Table 6 demonstrates that all are consistent within their 95% confidence limits of $r_+ \propto pH^{0.25}$ other than the enstatite data of Schott et al. (1981) and the diopside data of Knauss et al. (1993) at 25°C, whose 95% confidence limits are within 0.08 and 0.04, respectively of a -0.25 slope. Taking account of (1) the similarity of the pH dependence of the rates depicted in Figures 8 and 9, and (2) the similarity of their structures, it seems likely that exchange reactions among H^+ and the metal found in their M_2 sites also forms the precursor complexes that control the dissolution of the other pyroxene/pyroxenoid minerals. Assuming therefore that the constant temperature, forward dissolution rates of the pyroxene/pyroxenoid minerals ($r_{+,\text{pyx}}$) follow Eqn.

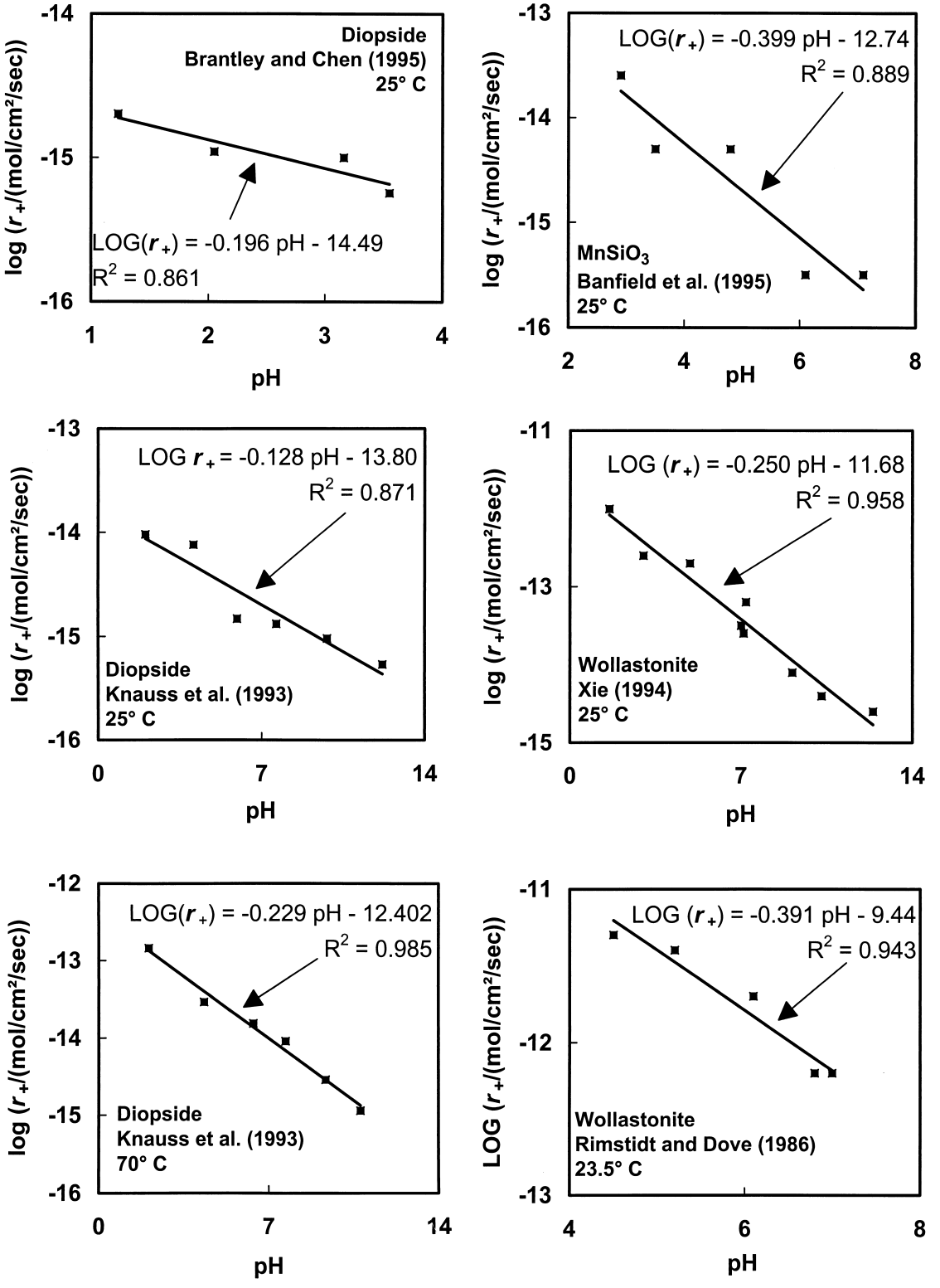

Fig. 9. Variation of the logarithms of pyroxene and pyroxenoid forward dissolution rates with pH. The symbols correspond to the experimental data reported in the indicated references and the curves correspond to a linear least squares fit of each data set—see text.

Table 6. Summary of selected experimentally measured pH dependence of pyroxene/pyroxenoid forward dissolution rates.

Mineral	Temperature °C	pH range	Number of observations	log (r_+)/pH[a]	R^2	Reference
Enstatite	25	2–7	3	−0.250 ± 1.78	0.750	Ferruzzi (1993)
Bramble Enstatite	25	1–6	3	−0.59 ± 0.26	0.998	Schott et al. (1981)
Bramble Enstatite	70	1.03–10.7	18	−0.206 ± 0.05	0.927	This study
Wollastonite	22.5	4.5–7	5	−0.39 ± 0.18	0.943	Rimstidt and Dove (1986)
Wollastonite	25	1.6–12.4	9	−0.249 ± 0.45	0.958	Xie (1994)
Diopside	25	2.03–12.2	6	−0.136 ± 0.07	0.871	Knauss et al. (1993)
Diopside	50	2.02–11.22	6	−0.168 ± 0.105	0.828	Knauss et al. (1993)
Diopside	70	2.06–10.74	6	−0.229 ± 0.03	0.984	Knauss et al. (1993)
Diopside	25	1.2–3.6	4	−0.196 ± 0.150	0.861	Chen and Brantley (1998)
Diopside	90	1.2–3.6	3	−0.766 ± 1.05	0.988	Chen and Brantley (1998)
$MnSiO_3$ (natural)	25	2.1–7.1	6	−0.399 ± 0.21	0.881	Banfield et al. (1995)

[a] The slopes, 95% confidence limits, and R^2 given in this table were generated by a least squares fit performed in the present study of the data reported indicated sources (see also Figs. 5 and 9). The slopes of these fits may, therefore differ from those reported by the original sources.

(5) where M_2^{z+} corresponds to the divalent cation found in the M_2 site and $n_4 = 1/8$ leads to

$$r_{+,\text{pyx}} = k_+\left(\frac{a_{H^+}^2}{a_{M_2^{2+}}}\right)^{1/8}. \quad (21)$$

This rate equation is also in agreement with the variation of wollastonite dissolution rates with aqueous calcium concentration; Rimstidt and Dove (1986) observed that their experimentally measured wollastonate dissolution rates were consistent with $r_{+,\text{wollastonite}} \propto C_{\text{tot,Ca}}^{0.08\pm0.07}$. This agreement further supports the application of the dissolution mechanism described above for enstatite to other pyroxene/pyroxenoid minerals. It should be re-emphasized that Eqn. 20 is based on the assumption that the mineral surface is undersaturated with respect to precursor complexes. It may be possible that at acidic pH and low aqueous M_2^{z+} activity these surface become saturated with precursor complexes, significant M_2^{z+} depleted layers form, and rates will reach a true dissolution plateau where the rates are independent of both pH and $a_{M_2^{2+}}$ (see Fig. 1). Such may be the case for wollastonite; Xie and Walther (1994) reported that the surfaces of acid leached wollastonite were so depleted in calcium that its surface properties were similar to those of microporous silica.

6. EXPERIMENTAL AND COMPUTATIONAL UNCERTAINTIES

Uncertainties associated with the rate constants generated above arise from a variety of sources, including the measurement of aqueous solution concentrations, fluid flow rates, and mineral surface areas. The uncertainties in the measured values of the total aqueous silica and magnesium concentration are on the order of ±4% or less for solutions containing >0.5 ppm Si and 0.1 ppm Mg; at lower concentrations the uncertainties are ±10%. Computational and experimental uncertainty in the pH of these solutions are ±0.1 pH units. Uncertainties in fluid flow rate measurements are not more than 2%. In contrast, the uncertainties associated with the B.E.T. surface area measurement of the enstatite powder is ±10%. In addition the mineral surface area changed somewhat over the duration of each experiment. To assess the temporal effects of changing mineral surface areas on the resulting dissolution rates, one of the final fluid flow rates for several of the mineral samples of a single fluid composition was set approximately equal to the first. The difference in the resulting fluid concentrations were on the order of 15% or less. A reasonable estimate of the relative uncertainty is the sum of the uncertainties associated with (1) the measurement of fluid compositions, (2) fluid flow rates, and (3) potential changes in enstatite surface area during the experiments. Considering the estimates of each of these contributions, the relative uncertainties among enstatite dissolution rates reported in the present study are ±20%. The overall uncertainties are somewhat higher, as they will also include the uncertainties associated with the B.E.T. surface area measurement of the enstatite powder. Taking this latter contribution into account, the overall uncertainties of the rates reported in this study are ±30%.

7. CONCLUSION

Enstatite dissolution rates measured at 70°C far from equilibrium conditions are found to be consistent with $r_+ \propto (a_{H^+}^2/a_{Mg^{2+}})^{1/8}$ over the pH range 1–11. This variation of rates with solution composition is interpreted to stem from its dissolution mechanism which proceeds via two major steps: (1) the exchange between $2H^+$ with the Mg located in the M_2 site of the enstatite structure, via the breaking of Mg–O bonds and forming neutrally charged rate controlling precursor complexes, followed by (2) the liberation of partially detached silica tetrahedra via the breaking of Si–O bonds. Consideration of their similar structure and rate variation with solution composition suggests that this mechanism also holds for all of the pyroxene/pyroxenoid minerals. As the rate controlling precursor complex is formed by hydrogen-metal exchange reactions, the variation of these rates with pH is governed by the speciation of the aqueous metal found in the mineral M_2 site, rather than the quantity of adsorbed protons, H_2O or OH^- on the mineral surface. Consequently, these rates do not minimize near the minerals pH_{zpc}. The rates and mechanisms of enstatite dissolution are compared with those of forsterite by Oelkers (1999).

Acknowledgments—We thank Jean-Louis Dandurand, Robert Gout, K. Vala Ragnarsdottir, David Sherman, Christophe Monnin, Sigurdur Gíslason, Patrica Fournier, Carlos Jové, Jean-Marie Gauthier, Oleg

Pokrovsky, Marwan Alkattan, and Stacey Callahan for helpful discussions during the course of this study. Jocelyne Escalier, Philippe de Parseval, Michael Thibaut, Oleg Pokrovsky, and Jean-Marie Gauthier provided expert technical assistance. Support from Centre National de la Recherche Scientifique is gratefully acknowledged.

Associate editor: T. Paces

REFERENCES

Aagaard P. and Helgeson H. C. (1977) Thermodynamic and kinetic constraints on the dissolution of feldspars. *Geol. Soc. Am. Abst. Prog.* **9,** 873.

Aagaard P. and Helgeson H. C. (1982) Thermodynamic and kinetic constraints on reaction rates among minerals and aqueous solutions: I. Theoretical considerations. *Am. J. Sci.* **282,** 237–285.

Banfield J. F., Ferruzzi G. C., Casey W. H., and Westrich H. R. (1995) HRTEM study comparing naturally and experimentally weathered pyroxenoids. *Geochim. Cosmochim. Acta* **58,** 19–31.

Berger G., Cadoré E., Schott J., and Dove P. (1994) Dissolution rate of quartz in Pb and Na electrolyte solutions. Effect of the nature of surface complexes and reaction affinity. *Geochim. Cosmochim. Acta* **58,** 541–551.

Berner R. A. (1995) Chemical weathering and its effect on atmospheric CO_2 and climate. *Rev. Mineral.* **31,** 565–583.

Berner R. A. and Schott J. (1982) Mechanisms of pyroxene and amphibole weathering. II. Observations of soil grains. *Am. J. Sci.* **282,** 1214–1231.

Berner R. A., Lasaga A. C., and Garrels R. M. (1983) The carbonate-silicate geochemical cycle and its effect on atmospheric carbon-dioxide over the past 100 years. *Am. J. Sci.* **283,** 641–683.

Blum A. E. and Stillings L. L. (1995) Feldspar dissolution kinetics. *Rev. Mineral.* **31,** 291–352.

Brady P. V. (1991) The effect of silicate weathering on global temperature and atmospheric CO_2. *J. Geophys. Res.* **B96,** 18,101–18,106.

Brady P. V. and Carroll S. A. (1994) Direct effects of CO_2 and temperature on silicate weathering. *Geochim. Cosmochim. Acta* **58,** 1853–1856.

Brantley S. L. and Chen Y. (1995) Chemical weathering rates of pyroxenes and amphiboles. *Rev. Mineral.* **31,** 119–172.

Casey W. H., Westrich H. R., Banfield J. F., Ferruzzi G., and Arnold G. W. (1993) Leaching and reconstruction at the surfaces of dissolving chain silicate minerals. *Nature* **366,** 253–255.

Chen Y. and Brantley S. L. (1998) Diopside and anthophyllite dissolution at 25°C and 90°C and acid pH. *Chem. Geol.* **147,** 233–248.

Chou L. and Wollast R. (1984) Study of the weathering of albite at room temperature and pressure with a fluidized bed reactor. *Geochim. Cosmochim. Acta* **48,** 2205–2217.

Chou L. and Wollast R. (1985) Steady state kinetics and dissolution mechanisms of albite. *Am. J. Sci.* **285,** 963–993.

Devidal J. L. (1994) Solubilité et cinétique de dissolution/précipitation de la kaolinite en milieu hydrothermal. Approche expérimentale et modélisation. Ph.D. thesis Université Paul Sabatier, Toulouse, France.

Devidal J. L., Schott J., and Dandurand J. L. (1997) An experimental study of kaolinite dissolution and precipitation kinetics as a function of chemical affinity and solution composition at 150°C, 40 bars, and pH 2, 6.8, and 7.8. *Geochim. Cosmochim. Acta* **61,** 5165–5186.

Doremus R. H. (1975) Interdiffusion of hydrogen and alkali ions in a glass surface. *J. Non-Cryst. Solids* **19,** 137–144.

Drever J. I. (1988) *The Geochemistry of Natural Waters*. Prentice-Hall.

Drever J. I. and Clow D. W. (1995) Weathering rates in catchments. *Rev. Mineral.* **31,** 463–483.

Ferruzzi G. G. (1993) The character and rates of dissolution of pyroxenes and pyroxenoids. MS thesis, University of California, Davis, CA.

Gautier J.-M., Oelkers E. H., and Schott J. (1994) Experimental study of K-feldspar dissolution rates as a function of chemical affinity at 150°C and pH 9. *Geochim. Cosmochim. Acta* **58,** 4549–4560.

Gautier J.-M., Oelkers E. H., and Schott J. (2001) Are quartz dissolution rates proportional to BET surface areas? *Geochim. Cosmochim. Acta* (in press).

Gislason S. R., Rose N. M., and Oelkers E. H. (1996) Chemical weathering, glaciers and the carbon cycle. In *Fourth International Symposium on the Geochemistry of the Earth's Surface*. (ed. S. H. Botterell), pp. 574–577. University of Leeds.

Helgeson H. C., Murphy W. M., and Aagaard P. (1984) Thermodynamic and kinetic constraints on reaction rates among mineral and aqueous solutions: II. Rate constants, effective surface area, and the hydrolysis of feldspar. *Geochim. Cosmochim. Acta* **48,** 2405–2432.

Johnson J. W., Oelkers E. H., and Helgeson H. C. (1992) SUPCRT92: A software package for calculating the standard molal properties of minerals gases, aqueous species and reactions among them from 1 to 5000 bars and 0 to 1000°C. *Comp. Geosci.* **18,** 899–947.

Koroleff F. (1976) Determination of silicon. In *Methods of Seawater Analysis* (ed. K. Grasshoff), pp. 149–158. Springer Verlag.

Knauss K. G., Nguyen S. N., and Weed H. C. (1993) Diopside dissolution kinetics as a function of pH, CO_2, temperature, and time. *Geochim. Cosmochim. Acta* **57,** 285–294.

Knauss K. G. and Wolery T. J. (1986) Dependence of albite dissolution kinetics on pH and time at 25°C and 70°C. *Geochim. Cosmochim. Acta* **50,** 2481–2497.

Knauss K. G. and Wolery T. J. (1989) Muscovite dissolution kinetics as a function of pH and time at 70°C. *Geochim. Cosmochim. Acta* **53,** 1493–1502.

Lartigue J.-E. (1994) Contribution à l'étude de l'altération des silicates: Approche expérimentale en milieu ouvert de la cinétique de dissolution à 25°C d'un pyroxène (Ca–Mg–Fe) en fonction du pH. Ph.D. thesis Université Aix-Marseille, France.

Lasaga A. C. (1981) Transition state theory. *Rev. Mineral.* **8,** 135–169.

Lasaga A. C., Soler J. M., Ganor J., Burch T. E., and Nagy K. L. (1994) Chemical weathering rate laws and global geochemical cycles. *Geochim. Cosmochim. Acta* **58,** 2362–2386.

Luce R. W., Bartlett W. B., and Parks G. A. (1972) Dissolution kinetics of magnesium silicates. *Geochim. Cosmochim. Acta* **36,** 35–50.

Marschester H. (1995) *Mineral Nutrition of Higher Plants*. Academic.

Murphy W. M. and Helgeson H. C. (1987) Thermodynamic and kinetic constraints on reaction rates among minerals and aqueous solutions. III. Activated complexes and the pH-dependence of the rates of feldspar, pyroxene, wollastonite, and olivine hydrolysis. *Geochim. Cosmochim. Acta* **51,** 3137–3153.

Murphy W. M. and Helgeson H. C. (1989) Thermodynamic and kinetic constraints on reaction rates among minerals and aqueous solutions. IV. Retrevial of rate constants and activation parameters for the hydrolysis of pyroxene, wollastonite, olivine, andalusite and quartz. *Am. J. Sci.* **288,** 17–101.

Murphy W. M., Pabalan R. T., Prikryl J. D., and Goulet C. J. (1996) Reaction kinetics and thermodynamics of aqueous dissolution and growth of analcime and Na-clinoptilolite at 25°C. *Am. J. Sci.* **296,** 128–186.

Nagy K. L. (1995) Dissolution and precipitation kinetics of sheet silicates. *Rev. Mineral.* **31,** 173–233.

Nagy K. L. and Lasaga A. C. (1992) Dissolution and precipitation kinetics of gibbsite at 80°C and pH 3: The dependence on solution saturation state. *Geochim. Cosmochim. Acta* **56,** 3093–3111.

Oelkers E. H. (1996) Summary and review of the physical and chemical properties of rocks and fluids. *Rev. Mineral.* **34,** 131–191.

Oelkers E. H. (1999) A comparison of enstatite and forsterite dissolution rates and mechanisms. In *Growth, Dissolution and Pattern Formation in Geosystems* (eds. B. Jamtveit and P. Meakin), pp. 253–268. Kewler Academic.

Oelkers E. H. (2001) An experimental study of forsterite dissolution as a function of temperature, and aqueous Mg and Si concentration. *Chem. Geol*. (in press).

Oelkers E. H. and Schott J. (1995a) Experimental study of anorthite dissolution and the relative mechanism of feldspar hydrolysis. *Geochim. Cosmochim. Acta* **59,** 5039–5053.

Oelkers E. H. and Schott J. (1995b) The dependence of silicate dissolution rates on their structure and composition. In *Water Rock Interaction* (eds. Y. K. Kharaka and O. V. Chudaev), pp. 153–156. A. A. Balkema.

Oelkers E. H. and Schott J. (1999) An experimental study of the dissolution rate of kyanite as a function of chemical affinity and solution composition. *Geochim. Cosmochim. Acta* **63,** 785–798.

Oelkers E. H., Schott J., and Devidal J. L. (1994) The effect of

aluminum, pH, and chemical affinity on the rates of aluminosilicate dissolution reactions. *Geochim. Cosmochim. Acta* **58,** 2011–2024.

Parks G. A. (1967) Aqueous surface chemistry of oxides and complex oxide minerals. In *Equilibrium Concepts in Natural Water Systems. Am. Chem. Soc. Adv. Chem. Ser.* **67,** 121–160.

Peck J. A., Farnan I., and Stebbins J. F. (1988) Disordering and the progress of hydration at the surface of diopside; a cross-polarisation MAS NMR study. *Geochim. Cosmochim. Acta* **52,** 3017–3021.

Petit J. C., Della M. G., Dran J. C., Schott J., and Berner R. A. (1987) Mechanism of diopside dissolution from hydrogen depth profiling. *Nature* **325,** 705–707.

Pokrovsky O. and Schott J. (2000) Kinetics and mechanism of forsterite dissolution at 25°C and pH from 1 to 12. *Geochim. Cosmochim. Acta* **64,** 3313–3325.

Ragnarsdottir K. V. (1993) Dissolution kinetics of heulandite at pH 2–12 and 25°C. *Geochim. Cosmochim. Acta* **57,** 2439–2449.

Ragnarsdottir K. V., Graham C. M., and Allen G. C. (1996) Surface chemistry of reacted heulandite determined by SIMS and XPS. *Chem. Geol.* **131,** 167–181.

Rimstidt J. D. and Dove P. M. (1986) Mineral/solution reaction rates in a mined flow reactor: Wollastonite hydrolysis. *Geochim. Cosmochim. Acta* **50,** 2509–2516.

Rosenthal R. and Rosnow R. L. (1984) *Essentials of Behavioral Research: Methods and Data Analysis*. McGraw-Hill.

Schlinder P. W. and Stumm W. (1987) The surface chemistry of oxides, hydroxides, and oxide minerals. In *Aquatic Surface Chemistry* (ed. W. Stumm), pp. 83–110. Wiley.

Schott J. and Berner R. A. (1983) X-ray photoelectron studies of the mechanism of iron silicate dissolution during weathering. *Geochim. Cosmochim. Acta* **47,** 2233–2240.

Schott J. and Berner R. A. (1985) Dissolution mechanisms of pyroxenes and olivines during weathering. In *The Chemistry of Weathering* (ed. J. I. Drever). NATO ASI series C; *Mathematical and Physical Sciences* **149,** 35–53.

Schott J., Berner R. A., and Sjoberg E. L. (1981) Mechanism of pyroxene and amphibole weathering—I. Experimental studies of iron-free minerals. *Geochim. Cosmochim. Acta* **45,** 2123–2135.

Schott J. and Oelkers E. H. (1995) Dissolution and crystallization rates of silicate minerals as a function of chemical affinity. *Pure Appl. Chem.* **67,** 603–610.

Schott J. and Petit J. C. (1987) New evidence for the mechanisms of dissolution of silicate minerals. In *Aquatic Surface Chemistry: Chemical Processes at the Mineral-Surface Interface* (ed. W. Stumm), pp. 293–315. Swiss Fed. Inst. Technol.

Siegel D. I. and Pfannkuch H. O. (1984) Silicate mineral dissolution at pH 4 and near standard temperature and pressure. *Geochim. Cosmochim. Acta* **48,** 197–201.

Sverdrup H. and Warfvinge P. (1993) Calculating field weathering rates using a mechanistic geochemical model—PROFILE. *J. Appl. Geochem.* **8,** 273–283.

Sverdrup H. and Warfvinge P. (1995) Estimating field weathering rates using laboratory kinetics. *Rev. Mineral.* **31,** 485–541.

Sverjensky D. A. (1994) Zero-point-of-charge prediction from crystal chemistry and solvation theory. *Geochim. Cosmochim. Acta* **58,** 3123–3129.

Wieland E., Werhli B., and Stumm W. (1988) The coordination chemistry of weathering: III. A potential generalization on dissolution rates of minerals. *Geochim. Cosmochim. Acta* **52,** 1969–1981.

Wolery T. J. (1983) EQ3NR, A computer program for geochemical aqueous speciation-solubility calculations: Users guide and documentation. UCRL-53414. Lawrence Livermore National Laboratory, Livermore, CA.

Xie Z. (1994) Surface properties of silicates, their solubility and dissolution kinetics. Ph.D. dissertation, Northwestern University, Evanston, IL.

Xie Z. and Walther J. V. (1994) Dissolution stoichiometry and adsorption of alkali and alkaline earth elements to the acid reacted wollastonite surface at 25 degrees C. *Geochim. Cosmochim. Acta* **58,** 2587–2598.